Author/s:
Modesti, D;Endrikat, S;García-Mayoral, R;Hutchins, N;Chung, D

Title:
Form-induced stress in turbulent flow over riblets

Date:
2018-01-01

Citation:
Modesti, D., Endrikat, S., García-Mayoral, R., Hutchins, N. & Chung, D. (2018). Form-induced stress in turbulent flow over riblets. Proceedings of the 21st Australasian Fluid Mechanics Conference, AFMC 2018, Australasian Fluid Mechanics Society.

Persistent Link:
https://hdl.handle.net/11343/252858

21st Australasian Fluid Mechanics Conference
Adelaide, Australia
10-13 December 2018

# Form-induced stress in turbulent flow over riblets

**D. Modesti[1], S. Endrikat[1], R. García-Mayoral[2], N. Hutchins[1] and D. Chung[1]**

[1]Department of Mechanical Engineering The University of Melbourne, Victoria 3010, Australia

[2]Department of Engineering, University of Cambridge, Cambridge CB2 1PZ, UK

## Abstract

We carry out direct numerical simulation of minimal open-channel flow over riblets. Several riblet geometries are simulated, namely symmetric triangular, asymmetric triangular, blade and trapezoidal, and with this unprecedented high-fidelity dataset, we are able to obtain broad insights into the flow physics of riblets. We find that the roughness sublayer thickness, above which the flow is statistically homogeneous, is proportional to the square root of the riblet groove cross-sectional area $\ell_g^+$ in both the drag-reducing and the drag-increasing regime, consistent with the ability of this parameter to collapse the roughness function corresponding to different groove geometries. Large grooves are associated with mean secondary velocities and they carry additional stress that contributes up to 40% of the total shear stress at the crest, comparable to the contribution from the turbulent fluctuations.

## Introduction

A large proportion of the energy required in transportation and pipe systems is used to overcome fluid-dynamic drag. In particular, skin friction constitutes 50% of the total drag on aircraft and almost all the drag in pipelines. Hence, reduction of skin friction can bring a substantial energy saving. Riblets are streamwise-aligned micro-grooves that can reduce drag by up to 10% in laboratory conditions [1], and are therefore considered one of the most promising techniques of passive drag reduction. The regime in which riblets reduce drag is referred to as the viscous or linear regime, as drag decreases linearly in this region with increasing riblet size. The linear mechanism is relatively well understood [6], whereas several mechanisms have been proposed to explain the disruption of the linear regime, which in one way or another can all be traced back to turbulence. In particular, two main physical mechanisms that contribute to the increase of the total stress have been identified. The first mechanism has been identified by García-Mayoral and Jiménez [3], who observed that large riblets trigger the onset of spanwise vortical structures, that are visible in the 2D premultiplied velocity spectrum right above the riblet crest, and are comparable to Kelvin–Helmholtz-like rollers which represent an additional contribution to the turbulent stress. Another mechanism is associated with non-zero mean secondary velocities over the riblets [4] which carry additional stress, often referred to as form-induced stress or dispersive stress [8], not to be confused with form (pressure) drag. Although the form-induced stress has been widely studied in flows over canopies and rough walls, its contribution to the total stress has never been quantified in flows over riblets. In this study we first attempt to understand how the geometry of the riblet groove relates to the height of the roughness sublayer and second, we investigate the contribution of the dispersive stress for various riblet geometries and sizes. For these purposes, we carry out direct numerical simulation (DNS) of minimal open-channel flow over several cross-sectional groove geometries, namely, symmetric and asymmetric triangles, blades and trapezoidals, each at a range of viscous scaled sizes.

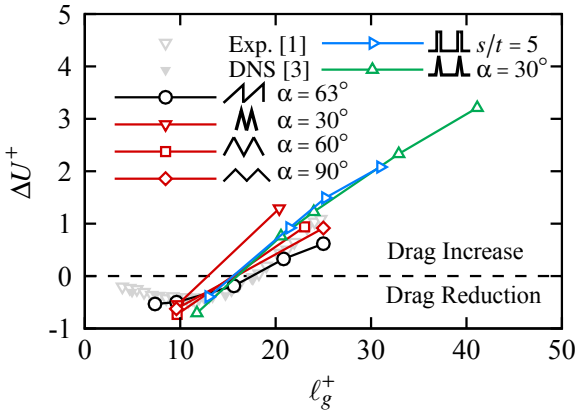


Figure 1: The roughness function $\Delta U^+$ as a function of the square root of groove cross-sectional area $\ell_g^+ = \ell_g/\delta_v$, where $\ell_g = \sqrt{A_g}$ and $\delta_v$ is the viscous length scale. $\alpha$ is the opening angle of the triangular and trapezoidal riblets and $s/t$ the spacing-to-thickness ratio.

## Methodology

We solve the incompressible Navier–Stokes equations with a uniform and constant kinematic driving pressure gradient $\Pi < 0$. The equations are discretized using an unstructured finite volume solver CTI Cliff, whereby variables are stored in a collocated node-based mesh [5]. We solve Navier–Stokes equations in a minimal open-channel domain [2] with dimensions $L_x \times L_y \times \delta$. Although small computational domains are known to produce unphysical results in the outer part of the flow, the unphysical region starts at a wall normal location $z_c$, which can be controlled by changing the spanwise length of the computational domain, $z_c \approx 0.4L_y$ [2]. The open-channel height $\delta$ is fixed, defined as the distance from the top flat surface to the mean height of the riblets. This guarantees that the mean wall-shear stress $\tau_w$ is fixed, for the same pressure gradient, $\tau_w = -\rho\Pi\delta$. The friction Reynolds number is fixed, $Re_\tau = \delta/\delta_v = 395$, where $\delta_v = \nu/u_\tau$ is the viscous length scale, $\nu$ is the kinematic viscosity of the fluid, $u_\tau \equiv \sqrt{\tau_w/\rho}$ the friction velocity and $\rho$ is the fluid density. The streamwise, spanwise and wall-normal directions are denoted as $x, y$ and $z$, respectively, and the velocity components in the corresponding directions are $u, v$ and $w$. Variables normalized with respect to wall units ($\delta_v$, $u_\tau$) are denoted with a + superscript. No-slip boundary conditions are imposed at the bottom riblet wall, whereas a free-slip impermeable boundary condition is imposed at the top boundary and periodicity is imposed in the streamwise and spanwise direction. We consider four riblet geometries (table 1), both in the drag decreasing and increasing regime, and compare them to a smooth open-channel flow. Different riblets geometries are indicated as TI$s^+$, AT$s^+$, BL$s^+$ and TA$s^+$, for symmetric triangle, asymmetric triangle, blade and trapezoid, respectively, where $s^+ \equiv s/\delta_v$, the viscous-scaled riblet spacing.

| | Case | $s^+$ | $\ell_g^+$ | $k^+$ | $\alpha$ | $\Delta x^+$ | $\Delta y^+{}_{min} - \Delta y^+{}_{max}$ | $\Delta z^+{}_{min} - \Delta z^+{}_{max}$ | $L_x^+$ | $L_y^+$ | $\Delta T u_\tau/\delta$ |
|---|---|---|---|---|---|---|---|---|---|---|---|
| Asymmetric triangular | | | | | | | | | | | |
| 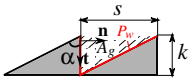 | AT15 | 15.0 | 7.50 | 7.50 | 63.4° | 6.54 | 1.50 – 5.00 | 0.40 – 6.00 | 1027 | 250 | 17.6 |
| | AT20 | 20.0 | 10.0 | 10.0 | 63.4° | 6.54 | 1.50 – 5.00 | 0.40 – 6.00 | 1027 | 250 | 42.8 |
| | AT30 | 30.0 | 15.0 | 15.0 | 63.4° | 6.54 | 1.50 – 5.00 | 0.40 – 6.00 | 1027 | 250 | 7.58 |
| | AT40 | 40.0 | 20.0 | 20.0 | 63.4° | 6.54 | 1.50 – 5.00 | 0.40 – 6.00 | 1027 | 250 | 37.7 |
| | AT50 | 50.0 | 25.0 | 25.0 | 63.4° | 6.54 | 1.50 – 5.00 | 0.40 – 6.00 | 1027 | 250 | 22.9 |
| Symmetric triangular | | | | | | | | | | | |
| 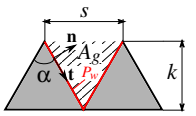 | TI10 | 10.0 | 9.75 | 18.8 | 30.0° | 6.00 | 0.0570 – 1.52 | 0.0334 – 7.02 | 1027 | 252 | 21.5 |
| | TI21 | 21.1 | 20.4 | 39.4 | 30.0° | 6.00 | 0.1190 – 3.18 | 0.2270 – 6.94 | 1027 | 253 | 29.4 |
| | TI15 | 15.0 | 9.68 | 12.7 | 60.0° | 6.00 | 0.0830 – 2.22 | 0.0408 – 7.05 | 1027 | 250 | 38.9 |
| | TI35 | 35.0 | 23.0 | 30.3 | 60.0° | 6.00 | 0.1610 – 4.93 | 0.0140 – 4.65 | 1027 | 245 | 53.3 |
| | TI19 | 19.2 | 9.60 | 9.60 | 90.0° | 6.00 | 0.1080 – 2.89 | 0.0471 – 7.06 | 1027 | 250 | 29.3 |
| | TI50 | 50.0 | 25.0 | 25.0 | 90.0° | 6.00 | 0.2300 – 7.05 | 0.0288 – 7.00 | 1027 | 250 | 88.0 |
| Blade | | | | | $s/t$ | | | | | | |
| 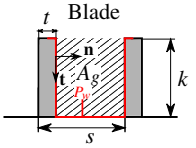 | BL20 | 20.5 | 12.9 | 10.1 | 5.00 | 6.00 | 1.00 – 2.00 | 0.300 – 7.00 | 1027 | 264 | 75.8 |
| | BL34 | 33.7 | 21.3 | 16.7 | 5.00 | 6.00 | 1.00 – 2.00 | 0.240 – 6.90 | 1027 | 266 | 98.3 |
| | BL40 | 39.6 | 25.0 | 19.5 | 5.00 | 6.00 | 1.00 – 2.00 | 0.300 – 6.90 | 1027 | 272 | 101 |
| | BL50 | 49.0 | 31.0 | 25.0 | 5.00 | 6.00 | 1.00 – 2.00 | 0.300 – 6.70 | 1027 | 294 | 46.9 |
| Trapezoidal | | | | | | | | | | | |
| 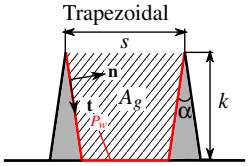 | TA18 | 17.9 | 11.8 | 8.93 | 30.0° | 6.00 | 1.50 – 5.00 | 0.800 – 6.00 | 2054 | 250 | 19.5 |
| | TA31 | 31.4 | 20.5 | 15.6 | 30.0° | 6.00 | 1.50 – 5.00 | 0.800 – 6.00 | 2054 | 250 | 29.0 |
| | TA36 | 36.5 | 24.0 | 18.2 | 30.0° | 6.00 | 1.50 – 5.00 | 0.800 – 6.00 | 2054 | 255 | 30.0 |
| | TA50 | 50.0 | 32.9 | 25.0 | 30.0° | 6.00 | 1.50 – 5.00 | 0.800 – 6.00 | 2054 | 250 | 29.4 |
| | TA60 | 62.0 | 41.1 | 31.3 | 30.0° | 6.00 | 1.50 – 5.00 | 0.800 – 6.00 | 2054 | 250 | 15.4 |

Table 1: DNS cases of minimal open-channel flow. $s^+ = s/\delta_v$ and $\ell_g^+ = \ell_g/\delta_v$, the viscous-scaled riblet spacing and square root of the groove area, $\ell_g = \sqrt{A_g}$. $\Delta x^+$ is the viscous-scaled mesh spacing in the streamwise direction and $\Delta y^+{}_{min} - \Delta y^+{}_{max}$, $\Delta z^+{}_{min} - \Delta z^+{}_{max}$ the minimum and maximum mesh spacing in the spanwise and wall-normal direction. $L_x^+$, $L_y^+$ are the viscous-scaled dimensions of the computational domain in the streamwise and spanwise directions, respectively. $\Delta T$ is the time-averaging interval.

### Drag Reduction

Drag reduction is usually quantified as the relative difference of the friction coefficient between smooth and riblet walls, $\mathcal{DR} = 1 - C_{fr}/C_{fs}$, where $C_{fs}$ and $C_{fr}$ are the skin-friction coefficients of the smooth and riblet walls, respectively, and $C_f \equiv 2\tau_w/(\rho U_0^2) = 2/U_0^{+2}$, where $U_0$ is the centreline velocity. Assuming matched $Re_\tau$, $\mathcal{DR} \sim \sqrt{2C_f}\Delta U^+$ [9] where $\Delta U^+ = U_{0s}^+ - U_{0r}^+ = \left(2/C_{fs}\right)^{1/2} - \left(2/C_{fr}\right)^{1/2}$, the velocity shift with respect to the smooth wall, also referred to as the Hama roughness function. A positive $\Delta U^+$ therefore indicates drag increase, whereas a negative $\Delta U^+$ indicates drag reduction. A similar relation can be obtained for constant bulk velocity [1, 3]. This relation shows that $\mathcal{DR}$ depends on the Reynolds number through the friction coefficient, thus 10% of drag reduction at $Re_\tau = 400$ is only 5% at $Re_\tau \sim 50{,}000$, typical of an aircraft [9], for $\Delta U^+ = -1$ (at the same $s^+$). Figure 1 shows $\Delta U^+$ from present DNS as a function of the viscous scale square root of the groove area $\ell_g^+ \equiv \ell_g/\delta_v$, where $\ell_g = \sqrt{A_g}$, compared to experiments [1] and previous DNS [3]. As already noted in previous studies [3], $\ell_g^+$ collapses the drag curve near to the optimum. A physical motivation for this behavior has been proposed [3], whereby a linear stability model for the riblet wall shows that $\ell_g^+$ can be related to the onset of a Kelvin–Helmholz-like instability over riblets.

### Dispersive stress and roughness sublayer

We use the double average, splitting the instantaneous fields into a mean and a fluctuating part, $\theta(x,y,z,t) = \overline{\theta}(y,z) + \theta'(x,y,z,t)$, and further decomposing the mean into $\overline{\theta}(y,z) = \langle\theta\rangle(z) + \widetilde{\theta}(y,z)$, where $\overline{\theta}$ indicates averaging in $t$, $x$ and riblet periods and $\langle\theta\rangle$ indicates the superficial average, i.e. $\langle\theta\rangle = (1/s)\int_0^s \overline{\theta}\mathrm{d}y$, where $\theta$ inside the solid is set to zero. Using this notation the Reynolds shear stress tensor can be written as, $\overline{uw}(y,z) = \overline{u'w'} + \overline{u}\,\overline{w}$ , where $\overline{u'w'}$ is the turbulent component of the Reynolds stress and $\overline{u}\,\overline{w}$ the dispersive or form-induced component. We first focus on the mean momentum balance equation,

$$\nabla\cdot\tau_D + \nabla\cdot\tau_T - \Pi = \nu\nabla^2\overline{u}, \tag{1}$$

where $\tau_D = (\overline{u}\,\overline{v}, \overline{u}\,\overline{w})$ and $\tau_T = (\overline{u'v'}, \overline{u'w'})$ are the dispersive and turbulent contributions to the mean momentum balance equation. Recently, Modesti *et al.* [7] interpreted (1) as a Poisson equation in which the terms at the left hand side are the source terms, obtained from DNS, and represent the contributions of dispersion, turbulence and pressure gradient to the mean velocity. Therefore $\overline{u}_D$, the solution of $\nabla\cdot\tau_D = \nu\nabla^2\overline{u}_D$, can be identified as the mean the velocity field induced by dispersion. On a smooth wall $\nabla\cdot\tau_D$ is zero, hence the solution of the associated Poisson equation directly allows to relate this source term with $\Delta U^+$. For this reason in figure 2 we report the viscous scaled dispersive stresses $\nabla\cdot\tau_D{}^+ \equiv \nabla\cdot\tau_D/(u_\tau^2/\delta_v)$ over the riblets, where positive values correspond to local drag increase and negative values to local drag reduction, as $\nabla\cdot\tau_D$ is negatively correlated to $\overline{u}_D$. All flow cases show that dispersion has a drag-increasing contribution at the crest, whereas it is drag-decreasing inside the groove. The figure shows that large riblets are characterized by large values of dispersion at the crest, suggesting a detrimental effect for drag reduction. Moreover, we focus on the roughness sublayer thickness $\delta_r$, that is the region of influence of the roughness element, above which the flow becomes homogeneous in the spanwise direction. Several definitions of roughness sublayer are available in literature, but the most common is the one that identifies $\delta_r$ as the wall-normal location at which the mean velocity profiles over the riblets col-

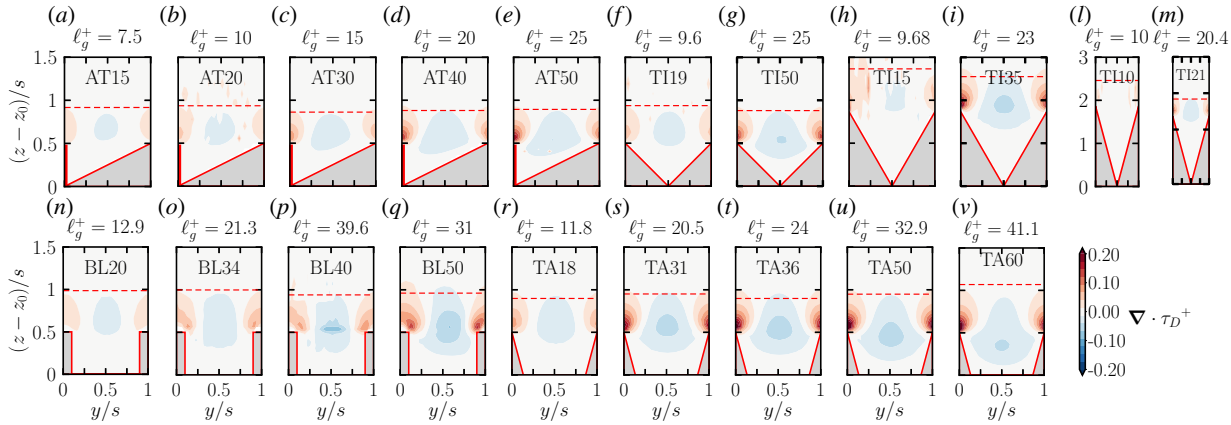


Figure 2: Dispersive stresses divergence $\nabla\cdot\tau_D{}^+ \equiv \nabla\cdot\tau_D/(u_\tau^2/\delta_\nu)$, see (1), over the riblets. The red dashed line indicates the location of the roughness sublayer $\delta_r$ as defined in (2). $z_0$ indicates the wall-normal coordinate of the riblet valley. Negative values indicate local drag reduction, positive values drag increase.

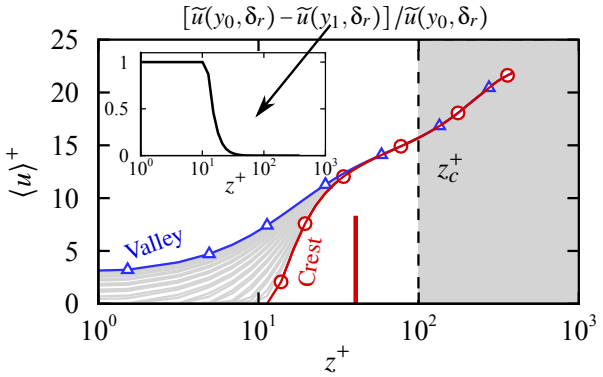


Figure 3: Mean velocity profile over the riblet for flow case TI50 (triangular $\alpha = 90°$, $\ell_g^+ = 25$). The vertical red line indicates the location of the roughness sublayer and the vertical dashed line indicates $z_c^+$. The inset shows the velocity difference between the valley and the crest, see (2). For symmetric triangular riblets $y_0$ and $y_1$ correspond to valley and crest.

lapse, within a reasonable threshold, i.e.

$$[\widetilde{u}(y_0,\delta_r)-\widetilde{u}(y_1,\delta_r)]/\widetilde{u}(y_0,\delta_r) \le 0.01, \qquad (2)$$

where $y_0$ and $y_1$ are the spanwise locations that identify the envelope of the mean velocity profiles over the riblets, see figure 3. It seems reasonable that the thickness of the roughness

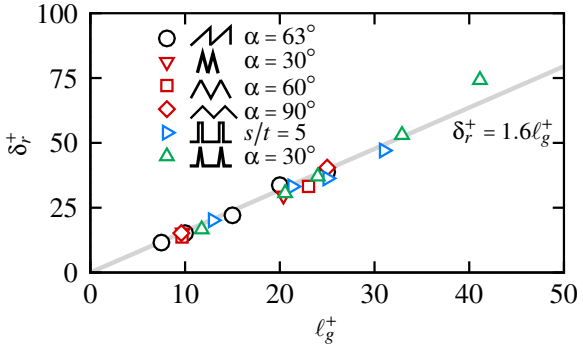


Figure 4: Roughness sublayer $\delta_r^+$ as a function of the square root of the groove area $\ell_g^+$, for all flow cases.

sublayer scales with the riblet spacing, but also with its geometry. Figure 4 shows that the roughness sublayer grows linearly with $\ell_g^+$, for all flow cases investigated here, following the relation $\delta_r^+ = 1.6\ell_g^+$. This finding relates the height of the roughness sublayer, which is a flow quantity, to a geometrical parameter of the groove. Note that in the Stokes (small-$\ell_g^+$) regime $\delta_r^+$ is a priori linearly proportional to $\ell_g^+$ (with a geometry dependent constant)[3]. This is consistent with the use of the parameter $\ell_g^+$ for collapsing the drag-reduction curves of different riblet geometries, both in the drag-decreasing and the drag-increasing regime (figure 1).

### Integrated Mean momentum balance in riblet groove

In this study we take the crest as indicative of the flow physics of the roughness sublayer and in particular we focus on the integrated mean momentum balance up to this height. To this end we integrate the streamwise mean momentum equation (1) over the riblet groove (hatched area in the sketches of table 1), and using the divergence theorem and the fact that the Reynolds stress is zero at the wall we obtain,

$$\tau_w/\rho = D + T + V + P, \qquad (3)$$

where $D = -\langle\widetilde{u}\widetilde{w}\rangle(z_t)$, $T = -\langle\overline{u'w'}\rangle(z_t)$, $V = \nu(\partial\langle u\rangle/\partial z)(z_t)$, $P = \Pi A_g/s$, are the dispersive, turbulent, viscous and pressure gradient contributions at the crest height $z_t$, which are balanced by the mean wall shear stress, $\tau_w/\rho = (1/s)\int_{P_w}\nu(\partial\overline{u}/\partial n)\mathrm{d}t$, where $P_w$ denotes the wetted wall perimeter of the groove (red line in the sketches of table 1, where $t$ and $n$ are the wall-tangential and wall-normal unit vectors). Figure 5 shows the different terms in (3), as a function of $\ell_g^+$. We note that the budget sums up to unity for all flow cases which highlights the good convergence of the flow statistics, apart for cases TA18 and TA31, for which a longer time averaging is still necessary. The viscous term is associated with the linear drag reduction mechanism [6] and it decreases almost linearly with $\ell_g^+$, consistent with the idea that riblets reduce the viscous stress by shifting upward the effective location of the wall [3]. For increasing riblet size, the turbulent and dispersive stresses at the crest become progressively larger, which is an indication that the flow at the riblet crest becomes turbulent. We note that the turbulent dispersion appears to play a relevant role, being always of the same order of magnitude of the turbulent stress or larger. In particular, for the largest trapezoidal grooves the turbulent dispersion is sensibly higher than the viscous and turbulent stress, contributing for more than 40% of the total stress at the crest. The figure also points out that $\ell_g^+$ can be interpreted as a local Reynolds number that is indicative of the status of the flow at crest. For

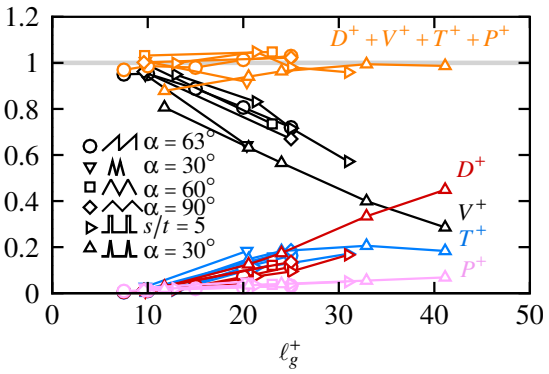


Figure 5: Integrated mean momentum budget up to the crest, see (3). Colors indicate different contributions: viscous $V^+$ (——), turbulent $T^+$ (——), dispersive $D^+$ (——), pressure gradient $P^+$ (——), total (——).

riblets with $\ell_g^+ \lesssim$ 11-12 the flow at the crest is laminar, as both turbulent and dispersive stresses are zero, whereas it becomes turbulent for $\ell_g^+ \gtrsim$ 11-12. This value of $\ell_g^+$ corresponds to the breakdown of drag reduction (1). Another picture of the physical mechanism can be drawn from figure 6 which shows the dispersive stress $D^+$ and the turbulent stress $T^+$ at the crest as a function of $\Delta U^+$. Both $D^+$ and $T^+$ are comparable in magnitude for all geometries, apart from the trapezoidal and the 30° triangular grooves. For the trapezoidal grooves (△, figure 6*b*) the higher intensity of $D^+$ has a detrimental effect on drag reduction (cf. figure 2*r*–*u*). The sharp triangular groove instead seems to suppress the turbulent dispersion, without increasing the turbulent fluctuations. Despite the interesting insight given by figures 5 and 6 this local analysis is only an indication, as it is limited to the plane of the crest, whereas $\Delta U^+$ depends on the three components of the Reynolds stress integrated over the entire wall layer, see (1). Moreover, a fair comparison with the smooth wall requires the knowledge of the equivalent location of the wall, that is, the protrusion height. These topics will be explored in the future.

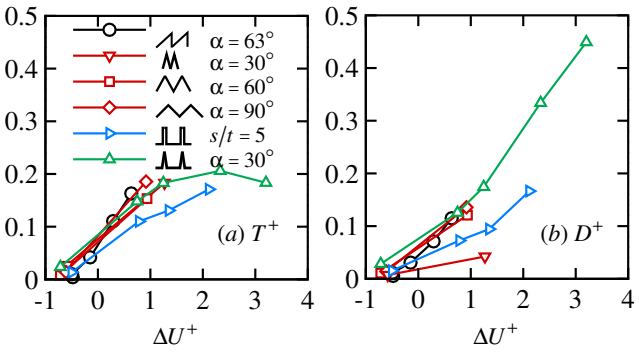


Figure 6: (*a*) Turbulent stress and (*b*) Dispersive stress at the crest as a function of $\Delta U^+$.

## Conclusions

We have performed DNS of minimal open-channel flow over riblets. The minimal open-channel flow configuration made it possible to accurately simulate, for the first time, several different groove geometries, allowing us to draw more general conclusions than in previous studies. We find that the roughness sublayer is a linear function of the square root of the groove area. This finding suggests that the effect of the groove geometry can be accounted for, with very good accuracy, by $\ell_g^+$, thus giving a possible physical motivation for the good collapse of the drag reduction curves when plotted against this parameter. This is consistent with the interpretation of $\ell_g^+$ as a local Reynolds number that indicates the status of the flow at the crest. In particular we find that local transition to turbulence occurs for $\ell_g^+ \approx$ 11-12, which also corresponds to the breakdown of drag reduction. Moreover, we observe that dispersive stresses have a drag-increasing contribution at the crest, that increases with the riblet size. They are found to have similar relevance or larger than the turbulent fluctuations, contributing up to 40% of the total stress at the crest. Despite some flow cases are not fully converged (see Table 1), we focused on distinct characteristics of the flow field and we expect these conclusions to be valid for fully converged statistics. Future studies will aim at further characterizing the role of turbulent dispersion in the breakdown of drag reduction and quantifying its contribution to $\Delta U^+$ by integrating this contribution across the wall layer.


## Acknowledgements

This research was supported by resources provided by The Pawsey Supercomputing Centre with funding from the Australian Government and the Government of Western Australia and by the National Computing Infrastructure (NCI), which is supported by the Australian Government. This research was partially supported under an Australian Research Council Discovery Project (DP170102595). This work has also benefit from useful discussion with Matteo Bernardini on unstructured data processing. Davide Modesti has been partially funded by Ermenegildo Zegna, through the "EZ Founder's Scholarship".


## References


[1] Bechert, D., Bruse, M., Hage, W., van der Hoeven, J. and Hoppe, G., Experiments on drag-reducing surfaces and their optimization with an adjustable geometry, *J. Fluid Mech.*, **338**, 1997, 59–87.

[2] Chung, D., Chan, L., MacDonald, M., Hutchins, N. and Ooi, A., A fast direct numerical simulation method for characterising hydraulic roughness, *J. Fluid Mech.*, **773**, 2015, 418–431.

[3] García-Mayoral, R. and Jiménez, J., Hydrodynamic stability and breakdown of the viscous regime over riblets, *J. Fluid Mech.*, **678**, 2011, 317–347.

[4] Goldstein, D., Handler, R. and Sirovich, L., Direct numerical simulation of turbulent flow over a modeled riblet covered surface, *J. Fluid Mech.*, **302**, 1995, 333–376.

[5] Ham, F., Mattsson, K. and Iaccarino, G., Accurate and stable finite volume operators for unstructured flow solvers, in *CTR Annual Research Briefs*, 2006, 243–261.

[6] Luchini, P., Manzo, F. and Pozzi, A., Resistance of a grooved surface to parallel flow and cross-flow, *J. Fluid Mech.*, **228**, 1991, 87–109.

[7] Modesti, D., Pirozzoli, S., Orlandi, P. and Grasso, F., On the role of secondary motions in turbulent square duct flow, *J. Fluid Mech.*, **847**, 2018, R1.

[8] Nikora, V., Goring, D., McEwan, I. and Griffiths, G., Spatially averaged open-channel flow over rough bed, *J. Hydraul. Eng.*, **127**, 2001, 123–133.

[9] Spalart, P. and McLean, J., Drag reduction: enticing turbulence, and then an industry, *Phil. Trans. R. Soc. A*, **369**, 2011, 1556–1569.